Capturing the Epistemic Uncertainty in Subduction Earthquake Rupture Parameters

A.M. Buenrostro[a,b,d*], F. Cotton[b,c], J. Jara[b], J.G.F. Crempien[a,d], R. Jünemann[a,d]

[a] Department of Structural and Geotechnical Engineering, School of Engineering, Pontificia Universidad Católica de Chile, Vicuña Mackenna 4860, Macul, Santiago, Chile.

[b] GFZ Helmholtz Centre for Geosciences, Telegrafenberg, 14473, Potsdam, Germany.

[c] Institute of Earth and Environmental Science, University of Potsdam, 14476, Potsdam, Germany.

[d] Research Center for Integrated Disaster Risk Management (CIGIDEN), Vicuña Mackenna 4860, Macul, Santiago, Chile.

*Corresponding author

Email address: ambuenrostro@uc.cl / ambo@gfz.de (Angelica Monserrat Buenrostro)

Declaration of interest statement

The authors declare that they have no known competing financial interests or personal relationships that could have appeared to influence the work reported in this paper.

Abstract

Subduction earthquakes are highly destructive and can trigger devastating tsunamis, highlighting the need for a consistent probabilistic seismic–tsunami hazard assessment. However, current approaches treat both hazards separately: tsunami models use coseismic slip distributions, while seismic models rely mostly on empirical ground-motion prediction equations. This creates inconsistencies because both depend on different representations of the source. Here, we address this inconsistency by systematically quantifying epistemic uncertainties in ground-motion simulations derived from kinematic rupture models based on slip distributions of large subduction earthquakes, enabling a common and physically consistent source representation for both hazards. We use the 2015 Illapel Mw 8.3 earthquake ground-motion in Central Chile as a test study. We test different rupture velocities, rise-time parameterisations, as well as hypocentre locations using two one-dimensional velocity models to capture the epistemic uncertainty of these kinematic rupture parameters and evaluate the impact on ground-motion. Our results show that rupture time, controlled by rupture velocity, is the main source of epistemic uncertainty. We compare the resulting simulations with the observed ground-motion at eight stations. Bias and RMSE decrease when adopting depth-dependent rupture velocities, with 0.3 of shear-wave velocity (Vs) in the shallow domain (<10 km) and 0.5Vs at depths greater than 15 km. Rupture velocity is then identified as the key parameter controlling ground-motion variability in kinematic source models. For this event, the simulations fit the observations better when the regional velocity model is used, and they more accurately reproduce ground-motion in the frequency band of 0.5-3 Hz.

Keywords: Epistemic uncertainties, Kinematic rupture propagation, Subduction earthquakes, Coseismic slip distribution, Central Chile.

1. Introduction

Subduction earthquakes pose a severe hazard to coastal populations, causing loss of life and substantial economic damage (Løvholt et al., 2012, 2015). Probabilistic seismic–tsunami hazard assessment, therefore, plays a crucial role in subduction zones. However, it remains a global challenge as seismic and tsunami hazard are often treated as independent phenomena, each based on different rupture representations for the same earthquake scenario (e.g., De Risi and Goda, 2016; Park et al., 2017; Goda et al., 2021). In practice, Ground Motion Prediction Equations (GMPEs) are used to estimate Earthquake Intensity Measures (EIMs), while tsunami intensity measures are estimated from numerical inundation models based on coseismic slip distributions, so that both hazards rely on different and often incompatible descriptions of the earthquake source, leading to inconsistencies (Figure 1a).

One way to mitigate this problem is to use the same coseismic slip distribution employed in tsunami inundation modelling to generate ground motion and derive EIMs. This ensures a consistent source representation for both hazards (Figure 1b). However, earthquake rupture along subduction interfaces is a complex process that strongly influences ground-motion characteristics (e.g., Yokota et al., 2011; Kurahashi and Irikura, 2013).

Translating a static slip model into a ground-motion simulation at a desired frequency, therefore, poses an additional challenge, as it requires defining a propagation rupture model. Fully dynamic rupture models have therefore been developed to simulate the physical processes governing earthquake rupture, incorporating friction laws, stress evolution, and energy dissipation. However, these models are often computationally expensive (e.g., Andrews, 1976; Madariaga et al., 1998; Andrews, 2005; Gabriel et al., 2012, 2013). To reduce this cost, some studies have proposed hybrid approaches, such as pseudo-dynamic models. Such models combine kinematic descriptions with physics-based constraints and dynamic rupture modelling (e.g., Guatteri et al., 2004; Crempien and Archuleta, 2017; Castro-Cruz and Mai, 2025).

Although these models better capture the physics of the rupture process, they are rarely used to constrain numerical simulations of tsunami inundation. This is mainly because tsunami modelling is primarily sensitive to the principal vertical deformation of the seafloor above the fault. As a result, a static Okada approach (Okada, 1985) is commonly adopted as a reasonable and computationally efficient approximation for tsunami inundation, thereby reducing the need for fully dynamic rupture simulations.

Instead of full dynamic rupture simulations, most tsunami applications then use stochastic slip distribution, which reproduces the variability and spectral characteristics of subduction earthquake slip distributions relevant to tsunami generation (e.g., Goda et al., 2015; Melgar et al., 2016; Cienfuegos et al., 2018; Crempien et al., 2020; Scala et al., 2020; Small and Melgar, 2023; Buenrostro et al., 2026).

To describe the space-time evolution of the rupture process needed for ground-motion simulations, a kinematic framework requires defining key rupture parameters, such as rupture time (t_{rup}), rupture velocity (V_r) and rise time (t_0). Such models commonly assume a constant V_r as a fraction of the shear-wave velocity (V_s), typically ranging from 0.8 to 0.9 (e.g., Heaton, 1990; Herrero and Bernard, 1994; Ruiz et al., 2011; Venegas-Aravena, 2023).

However, most applications that adopt stochastic slip distributions and a kinematic rupture process focus on crustal earthquake scenarios, mostly located in California (e.g., Graves and Pitarka, 2010, 2015, 2016; Pitarka et al., 2022).Some approaches, such as those by Melgar et al. (2016), extend these methods to subduction-zone earthquakes, primarily for tsunami hazard assessments. Their model adopts depth-dependent rupture velocities from Graves and Pitarka (2010, 2015), rise-time scaling from Somerville et al. (1999), and variable hypocentre locations. In general, these methods, called semi-kinematic methods, follow similar procedures to generate stochastic slip distributions. However, the main source of epistemic uncertainty lies in the kinematic rupture parameters, particularly in V_r, t_0 , and hypocentre location, which remain poorly constrained by observations and the impact of these uncertainties is not evaluated.

To address this concern, in this study, we quantify epistemic uncertainties in ground-motion simulations using kinematic rupture models from slip distributions. As a case study, we use the 2015 Illapel Mw 8.3 earthquake in Central Chile. We explore different formulations for t_{rup}, which depends on V_r, t_0 and hypocentre location following previous empirical and theoretical studies, as well as our proposed approach (e.g., Heaton, 1990; Somerville et al., 1999; Mai et al., 2005; Di Toro et al., 2011; Graves and Pitarka, 2015 ; Melgar et al., 2016; Melgar and Hayes, 2017, 2019; Goldberg and Melgar, 2020; Goldberg et al., 2022). Such parameters are evaluated using two one-dimensional (1D) velocity models representing subduction-zone crustal structures (CRUST 2.0: Bassin et al., 2000; Central Chile: Caballero et al., 2023) to assess their effects on the simulated ground-motion at eight near-field stations.

We simulate ground-motions up to 2 Hz and band-pass filter both observed and simulated records between 0.1 and 1 Hz. By comparing observed and simulated geometric-mean response spectra, we evaluate the sensitivity of ground-motion predictions to the assumed rupture process and velocity structure, calculating metrics such as bias, Standard Deviation (SD) of residuals, and Root Mean Square Error (RMSE). Additionally, we test whether the ground-motion of a single event, such as the 2015 Illapel earthquake, is captured by the range of simulations. For this, we analyse the Probability Density Functions (PDFs) from all filtered simulation cases for several EIMs, including Peak Ground Acceleration (PGA) and Spectral Accelerations (SA) at 0.5, 2.0, and 10.0 s. Finally, we perform a frequency reliability analysis of the simulations on the models which are showing the best fit to the data, evaluating both the bias factor and the SD of residuals.

Our approach provides a novel framework that links kinematic rupture modelling with epistemic uncertainty quantification, bridging seismic and tsunami hazard assessment by adopting a common source description and reducing epistemic uncertainty by identifying and constraining the rupture parameters that control ground-motion variability, thereby enabling consistent physics-based scenarios for probabilistic hazard analysis in subduction zones.

2. Methodology

2.1. Kinematic rupture process

We address the inconsistency in conventional seismic-tsunami hazard assessment by proposing a unified framework that incorporates a kinematic rupture process, thereby ensuring consistency between the two hazards (Figure 1). We introduce a workflow through a logic tree approach (Figure 2: Step 1) that evaluates the variability of key kinematic parameters: t_{rup}, V_r, t_0 and hypocentre location using two different 1D velocity models. As a case study, we use the rupture characteristics and ground-motion variability of the 2015 Illapel Mw 8.3 megathrust earthquake in Central Chile.

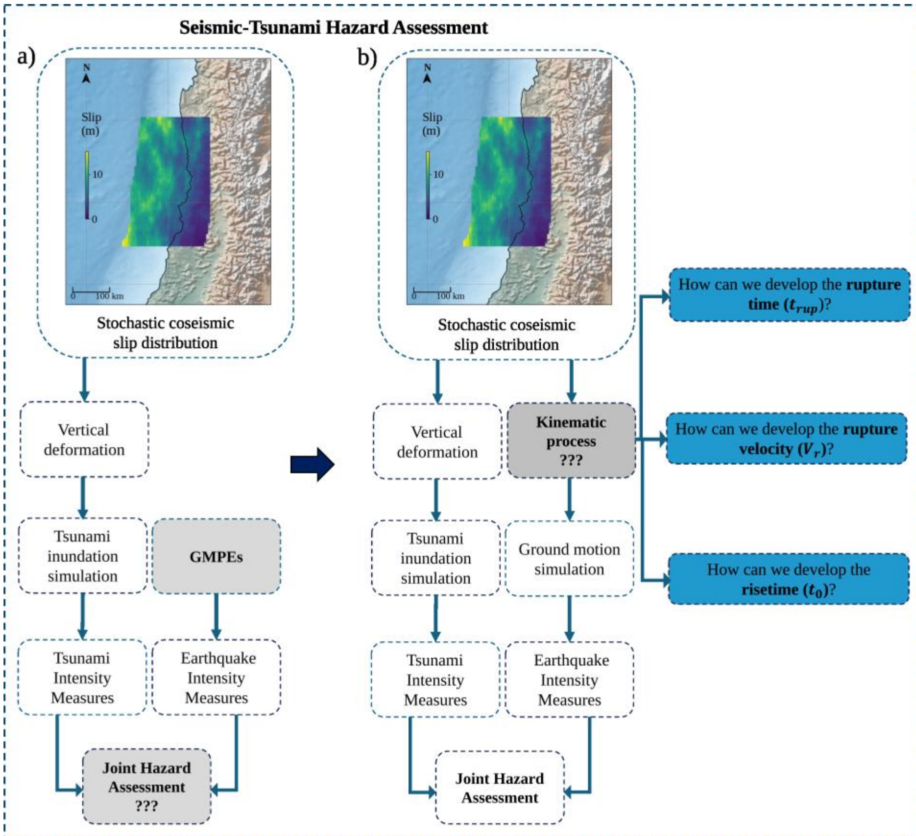

Figure 1. Seismic–tsunami hazard assessment: a) conventional approach, where tsunami and earthquake intensity measures are derived from independent source representations; b) proposed framework introducing a kinematic rupture process, enabling both hazards to originate from the same stochastic slip distribution (modified from Buenrostro et al., 2025). The framework requires defining the key kinematic parameters: rupture time (t_{rup}), rupture velocity (V_r) and rise time (t_0).

2.1.1. Coseismic slip distribution

We use the coseismic slip distribution derived from the inversion framework presented by the U.S. Geological Survey (USGS: see Data and Resources) as input for the kinematic process (Figure 2, Step 1). The finite fault plane extends 300 km along strike and 158.4 km down dip, with a spatial resolution of 12 km along strike and 8.8 km down dip, resulting in 450 subfaults.

Each subfault represents a discrete slip element within the fault plane. We adopt the focal mechanism parameters from the USGS inversion.

Because we use the final slip distribution at each subfault, the local slip direction is not explicitly defined. The slip direction varies spatially during rupture and cannot be assumed to be constant (e.g., Cotton and Campillo, 1995; Guatteri and Cocco, 1996). To account for these local variations, we estimate the rake for each subfault following the approach of Graves and Pitarka (2016) and Melgar et al. (2016), with a mean rake angle of 105°, consistent with the overall rake of the earthquake.

2.1.2 Velocity models

We estimate Green's functions for two 1D velocity models (Figure 2, Step 1) representing subduction-zone crustal structures: the CRUST 2.0 model (Bassin et al., 2000) and a regional model for Central Chile (Caballero et al., 2023). Key kinematic parameters: t_{rup}, V_r, t_0 and hypocentre location defined in the logic tree are evaluated for both models.

2.1.3. Rupture time and rupture velocity

We calculate the t_{rup} using Eq. (1), defined as the time when rupture initiates at the nucleation point and propagates radially across the fault plane. For each subfault, the rupture time t_{rup} depends on the distance d_i to the hypocentre and the average rupture velocity $\bar{V}_{r,i}$ along the propagation path,

$$t_{\mathrm{rup},i} = \frac{d_i}{\bar{V}_{r,i}}. \qquad (1)$$

To capture epistemic uncertainty in rupture propagation, we test five different V_r models, all defined as a fraction of V_s. These models control the spatiotemporal evolution of the rupture and allow a systematic evaluation of how V_r influence near-field ground-motion. The first case adopts a depth-dependent scaling, z, for subduction proposed by Melgar et al. (2016),

$$V_r = \begin{matrix} 0.56\,V_s, & z < 10 \text{ km}, \\ 0.80\,V_s, & z > 15 \text{ km}. \end{matrix} \quad (2)$$

The second case follows a common assumption in kinematic modelling, where V_r is constant (Heaton, 1990),

$$V_r = 0.80\,V_s. \quad (3)$$

The third case applies the subduction scaling of Goldberg and Melgar (2020),

$$V_r = \begin{matrix} 0.49\,V_s, & z < 10 \text{ km}, \\ 0.65\,V_s, & z > 15 \text{ km}. \end{matrix} \quad (4)$$

The fourth case employs the USGS model for the Illapel earthquake according to Goldberg et al. (2022), which incorporates an average rupture velocity ($\bar{V_r}$) of 1.5 km/s and a depth-dependent scaling,

$$V_r = \begin{matrix} 0.28\,V_s, & z < 10 \text{ km}, \\ 0.40\,V_s, & z > 15 \text{ km}. \end{matrix} \quad (5)$$

The last case defines our preferred model, as it yields an $\bar{V_r}$ of approximately 2 km/s, consistent with regional studies (e.g., Riquelme et al., 2020). This model also includes a depth-dependent scaling following,

$$V_r = \begin{matrix} 0.30\,V_s, & z < 10 \text{ km}, \\ 0.50\,V_s, & z > 15 \text{ km}. \end{matrix} \quad (6)$$

2.1.4. Rise time

We test four alternative cases for t_o, which is the duration of the slip. In the first three cases, t_o follows the formulation of Graves and Pitarka (2010), where the local t_o of each subfault, τ_{o_i} , scales with the square root of slip, $s_i^{1/2}$, and varies with depth according to Kagawa et al. (2004). For subduction earthquakes, we apply the modification proposed by Melgar et al. (2016), which adjusts the depth-dependent limits,

$$\tau_{o_i} = \begin{matrix} 2k\, s_i^{1/2}, & z < 10 \text{ km}, \\ k\, s_i^{1/2}, & z > 15 \text{ km}, \end{matrix} \quad (7)$$

Assuming a linear transition between 10 and 15 km. The proportionality constant k is determined by the average rise time, t_a, over the entire fault matches a target rise time. This t_a is defined by empirical relations between t_0 and seismic moment (M_0) in $N \cdot m$. We test three formulations for t_a. The first is prescribed by Somerville et al. (1999),

$$t_a = 4.308 \times 10^{-7} M_0^{1/3}. \quad (8)$$

The second relation, from Graves and Pitarka (2015), introduces a geometry-dependent scaling factor,

$$t_a = \alpha_\tau\, 3.124 \times 10^{-7} M_0^{1/3}, \quad (9)$$

where $\alpha_\tau$depends on dip and rake. The third is the formulation from Melgar and Hayes (2017),

$$t_a = 4.74 \times 10^{-6} M_0^{0.293}. \quad (10)$$

As a fourth case, we test the formulation of Di Toro et al. (2011), assuming a constant slip rate, $\dot{S}$, of approximately 1 m/s, and taking directly from this relation the t_0,

$$\dot{S} = s_i / t_0 \sim 1 \text{ m/s}, \quad (11)$$

$$t_0 = s_i / 1 \text{ m/s}. \quad (12)$$

2.1.5. Hypocentre location

We test three assumptions for hypocentre locations, enabling us to quantify the sensitivity of rupture directivity and ground-motion to the assumed nucleation position.

In the first case, the nucleation point is fixed at the observed hypocentre of the Illapel earthquake, located at latitude -31.5952°, longitude -71.6728° and a depth of 29.0 km. This case has the limitation that it cannot be used in future earthquakes. The second case follows the recommendation by Mai et al. (2005), locating the hypocentre at latitude -31.847°, longitude -

72.4994 and depth of 3.215 km. The hypocentre is located within a high-slip region but not at the point of maximum slip,

$$\frac{1}{3}D_{\max} < D_i < \frac{2}{3}D_{\max}, \tag{13}$$

where $D_{\max}$ is the maximum slip of the source model and D_i is the slip of each subfault.

The third case is based on Melgar and Hayes (2019). Here, the hypocentre is selected randomly using an exponential PDF constrained by observations, located at latitude -31.6343°, longitude -71.2357° and a depth of 31.865 km.

2.1.6. From Low-Resolution to High-Resolution Rupture Modelling

The finite-fault model used in this study comes from a low-frequency inversion. Its spatial resolution limits the ability to capture high-frequency rupture behaviour (Hartzell, 1989). To address this, we refine the fault-plane discretisation by subdividing each subfault into point sources, following the approach of Spudich and Archuleta (1987). The minimum wavelength, $\lambda_{\min}$, is defined as follows,

$$\lambda_{\min} = \frac{V_{s,\min}}{F_{\max}}, \tag{14}$$

where $V_{s,\min}$is the minimum shear-wave velocity and $F_{\max}$is the maximum target frequency considered in the simulation. The minimum point source spacing, $d_{e,\min}$, which controls the total number of point sources across the fault plane, is given by,

$$d_{e,\min} = \frac{\lambda_{\min}}{5}. \tag{15}$$

Once the grid is refined, the M_0 is interpolated across the rupture area. The t_{rup} at each point source depends on its distance from the hypocentre, ensuring a consistent spatiotemporal evolution of the rupture propagation at higher resolution.

2.2. Ground-Motion simulations

We simulate ground-motion at eight near-field stations of the Chilean Seismological Service (CSN: Figure 3), computing numerical Green's functions for the two 1D velocity models, CRUST 2.0 and Central Chile, using the Fomosto module of Pyrocko (Heimann et al., 2019; Figure 2: Step 2). The sampling rate is twice the maximum target frequency, which is 2 Hz, consistent with the discretisation of the subfaults, which avoids aliasing effects and ensures numerical stability and accurate interpolation during the convolution of the sources. Additionally, to represent the local slip-time history, we adopt a triangular source time function. This choice is consistent with the near-triangular moment rate evolution observed in large subduction earthquakes (Meier et al., 2017), supporting a physical description of the rupture process.

Once the ground-motions are computed we calculate the geometric-mean of observed and synthetic response spectral accelerations within a 0.1–1 Hz bandpass-filtered frequency range. We then quantify epistemic uncertainty (Figure 2: Step 3) across simulation cases by evaluating the mean $\ln(bias)$, defined as mean of $\ln(obs/syn)$. To characterize the error, we compute the SD of residuals and the $RMSE$ defined as,

$$RMSE = \sqrt{\frac{1}{n}\sum_{i=1}^{n}(obs_i - syn_i)^2}. \quad (16)$$

After evaluating the uncertainties, we compare the synthetic and observed data to access how well the simulation reproduces the ground motions of a well-recorded subduction earthquake and to identify up to which frequency our simulations are reliable (Figure 2, Step 4). The results of the workflow proposed in Figure 2 are presented in the section 3.

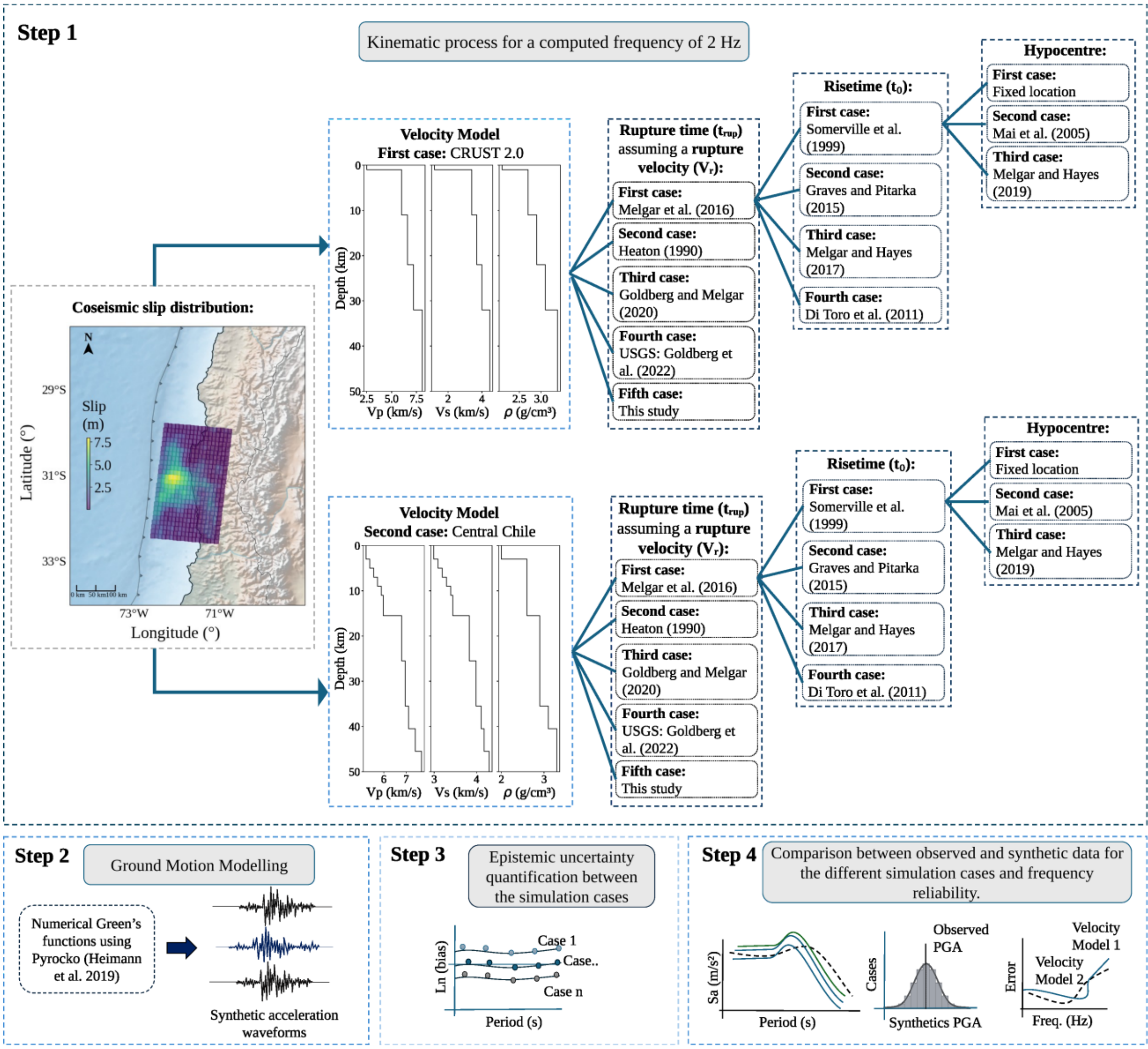

Figure 2. Workflow to evaluate epistemic uncertainty in kinematic rupture parameters using slip distributions from subduction earthquakes. Step 1: logic tree, composed of 24 branches, evaluating different rupture parameter cases. The input of this analysis is the coseismic slip distribution from the USGS inversion of the 2015 Illapel Mw 8.3 earthquake. Two 1D velocity models are tested, each simulating a kinematic rupture process up to 2 Hz, while varying rupture velocity (V_r), to constrain rupture time (t_{rup}), rise time(t_0), and hypocentre location based on different studies and this work; Step 2: ground-motion modelling using numerical Green's functions to generate synthetic acceleration waveforms; Step 3: quantification of epistemic

uncertainty between the simulation cases, evaluating bias and error. Step 4: comparison between the geometric-mean of observed and synthetic response spectral accelerations, in a bandpass filtered frequency range of 0.1 to 1 Hz, across the eight near-field stations, followed by a reliable frequency range assessment.

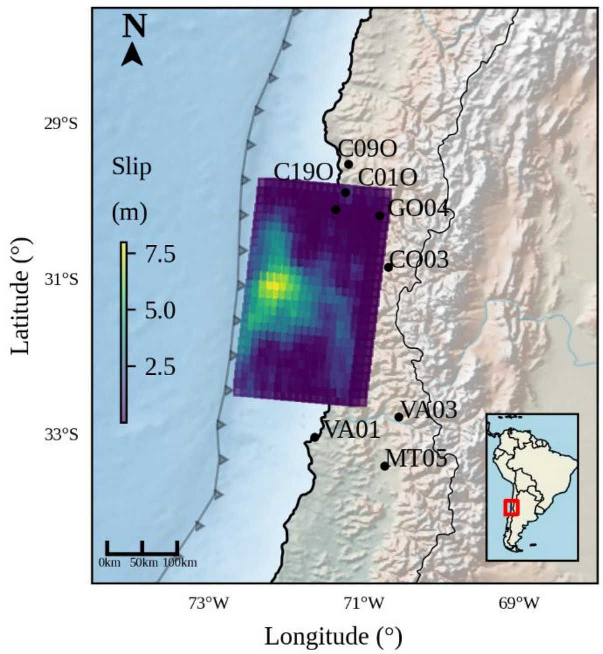

Figure 3. Spatial distribution of near-field strong-motion stations from the Chilean Seismological Service (CSN) used in this study, together with the coseismic slip distribution of the 2015 Illapel Mw 8.3 earthquake.

3. Results and Discussion

3.1. Sensitivity Analysis of Kinematic Rupture Parameter Cases

We evaluate all rupture parameter cases included in the logic tree (Figure 2, Step 1) and detailed in the methodology section. Figure 4 summarises the ensemble of the 24 logic-tree branches (V_r, t_0, and hypocentre location variations) and how they influence the rupture propagation across the fault plane. The full branches define the total epistemic uncertainty explored in this study.

Overall, Figure 4 shows considerable variability among the branches, both in the time ranges for the t_{rup} and t_0, as well as in the propagation of rupture across the different formulations used. However, across all parameter variations, the two 1D velocity models, CRUST 2.0 (Figures 4a-c) and Central Chile (Figures 4d-f), produce similar rupture-propagation behaviour, suggesting that the choice of the velocity model has only a minor influence on the kinematic rupture results. Examining the contribution of each branch of the logic tree, Figures 4a and 4d illustrate the impact of the V_r formulation on rupture evolution. Models proposed by Melgar et al. (2016) and Heaton (1980) yield similarly fast rupture propagation, with a t_{rup} of about 80 s. This similarity arises because, although Melgar et al. (2016) prescribe a depth-dependent V_r following the recommendations of Graves and Pitarka (2010, 2015), both parameterisations effectively converge to a nearly constant $V_r = 0.80\ V_s$. From a practical perspective, choosing between these two formulations may be of minor importance for kinematic source modelling. The formulation by Goldberg and Melgar (2020) is also close to Melgar et al. (2016) and Heaton (1980), but it tends to produce slightly slower rupture propagation. By contrast, the USGS formulation and the model introduced in this study prescribe overall lower V_r, leading to systematically longer rupture durations across the fault plane. All these formulations have been tested in subduction earthquake simulations, yet our results show maximum t_{rup} ranging from ~80 s to more than 150 s. This variability indicates that V_r is still not well understood and as noted in the Introduction, requires additional physical observations to be better constrained.

Figures 4b and 4e show similar spatial patterns in t_0 distributions, which are controlled by the slip, reflecting the common assumption in the four formulations and consistent with the physics of the rupture. Despite using the same fast V_r model (Melgar et al., 2016), the Somerville et al. (1999), Graves and Pitarka (2015), and Melgar and Hayes (2017) formulations produce considerable variability in the absolute t_0 values, showing a stronger sensitivity to the definition of t_a. However, t_a is dependent on the M_0, this dependence is implemented differently in each formulation: in Somerville et al. (1999), it is related to the distance from the hypocentre to the nearest asperity, in Graves and Pitarka (2015) involves the focal mechanism, and in Melgar and Hayes (2017) it is linked to the mean rise time derived from kinematic inversions of multiple inverse large earthquakes. In contrast, the Di Toro et al. (2011) distribution yields $t_0$values that are approximately proportional to slip, because it implicitly assumes a fast $\dot{S}$ on the order of ~ 1 m/s. Interestingly, its spatial pattern remains very similar to the other formulations. Overall, such differences in how each formulation parameterizes $t_a$and the $\dot{S}$ drive the variability in the resulting $t_0$distributions.

We show the influence of hypocentre location cases in Figures 4c and 4f. The approach of Mai et al. (2005) produces a slower rupture, which is expected to result in a weaker directivity. In contrast, the fixed case, corresponding to the observed hypocentre of the Illapel earthquake and the Melgar and Hayes (2019) case generate a similar fast rupture, despite their different nucleation points. This result confirms that rupture propagation and directivity effects are sensitive to the assumed nucleation point. In both the fixed case, which corresponds to the observed mainshock location, and the Melgar and Hayes (2019) case, the hypocentre is located within a high-slip region but not at the maximum-slip, consistent with the Mai et al. (2005) assumption.

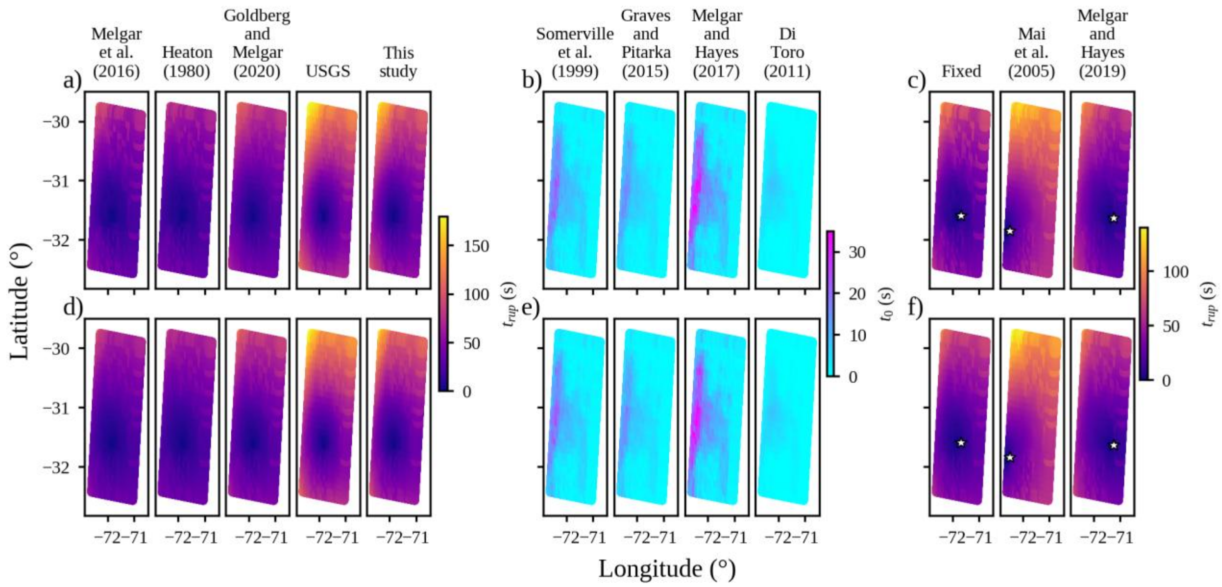

Figure 4. Kinematic rupture models for the Mw 8.3 Illapel earthquake computed at 2.0 Hz: a), d) rupture time (t_{rup}) distributions for all rupture velocity (V_r) formulations; b), e) rise time (t_0) distributions; c), f) t_{rup} distributions across all tested hypocentre locations; a-c) use the CRUST 2.0 1D velocity model (Bassin et al., 2000) and d-f) use the Central Chile 1D velocity model (Caballero et al., 2023).

Using the kinematic rupture models forementioned, we compute synthetic acceleration waveforms using numerical Green's functions across the eight near-field stations. For all stations, we calculate the geometric-mean response spectra of the synthetic and observed horizontal acceleration components in a bandpass filter frequency range of 0.1 to 1 Hz. Using these response spectra, we compute the mean $\ln(bias)$, to capture the epistemic uncertainty associated with each branch of the logic tree and quantify whether our simulations tend to overestimate or underestimate the observed ground-motion. We then summarise the logic-tree ensemble by computing the ensemble mean $\ln(bias)$ and the ±1 SD across the 24 realisations, which captures the variability associated with all rupture parameters and for both 1D velocity models (Figure 5).

In the period range analysed (~0.5–10 s), the ensemble mean shows relatively small bias at short periods, particularly for periods shorter than ~2 s, where ln(bias) remains close to zero. At intermediate periods, the ensemble mean becomes increasingly negative, with most realisations exhibiting a systematic negative ln(bias) between ~4 and 7 s, indicating an overestimation of the observed spectral amplitudes in this band. Two cases show a pronounced deviation at periods shorter than ~3 s, indicating an underestimation. Overall, the observations are covered by the range of simulations, as the dispersion of ln(bias) across the 24 realisations remains distributed around zero over most of the analysed period range.

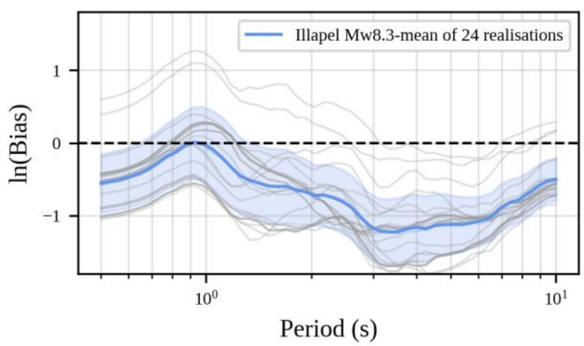

Figure 5. Bias in the geometric-mean horizontal response spectra, expressed as ln(bias) residuals between synthetics and observations for the 24 realisations in the logic-tree ensemble in a band-pass filter range of 0.1–1.0 Hz. Thin grey lines show, for each realisation, the mean ln(bias) averaged over the eight stations, the thick line shows the ensemble mean, and the shaded envelope indicates ±1 Standard Deviation (SD) across the realisations.

Figure 6 shows period-dependent model performance for each logic-tree branch, summarized by ln(bias) and the mean residual SD. To isolate the influence of V_r, we vary only this parameter while keeping the Somerville et al. (1999) t_0 model and a fixed hypocentre location (real case for Illapel earthquake), as is shown in the logic tree of Figure 2: Step 1. The V_r formulations produce the largest variability (Figures 6a and 6d), particularly when using the CRUST 2.0 model (Figure

6a). The variation is significantly larger for this parameter than for t_0 or hypocentre location. Additionally, we find that the mean ln(bias) exhibits stronger period-dependent variability.

For the t_0 variations, we fix the V_r model of Melgar et al. (2016) and a fixed hypocentre (Figure 2, Step 1). In contrast to V_r, the t_0 cases show remarkably low variations (Figures 6b and 6e). The SD of residuals remains almost constant across periods, and the mean log-bias curves cluster tightly around zero for the Central Chile velocity model (Figure 6e).

For the hypocentre location cases, we use the Melgar et al. (2016) V_r model and the Somerville et al. (1999) t_0 model (Figure 2, Step 1). The hypocentre formulations (Figures 6c and 6f) show an intermediate sensitivity: the variability is larger than for t_0 but smaller than for V_r. As with the other parameters, the CRUST 2.0 model yields broader scatter than the Central Chile model. Even so, the mean ln(bias) curves remain relatively consistent across the different hypocentre assumptions, supporting the suitability of the approaches by Mai et al. (2005) and Melgar and Hayes (2019) for future scenarios.

Across all parameter variations, the use of the Central Chile velocity model produces slightly lower epistemic uncertainty, the SD of residuals is marginally smaller than in the CRUST 2.0 model, and the mean ln(bias) curves lie closer to zero, particularly in the t_0 and hypocentre cases (Figures 6e and 6f). The improvement is modest but indicates that the regional structure yields more stable and less biased predictions.

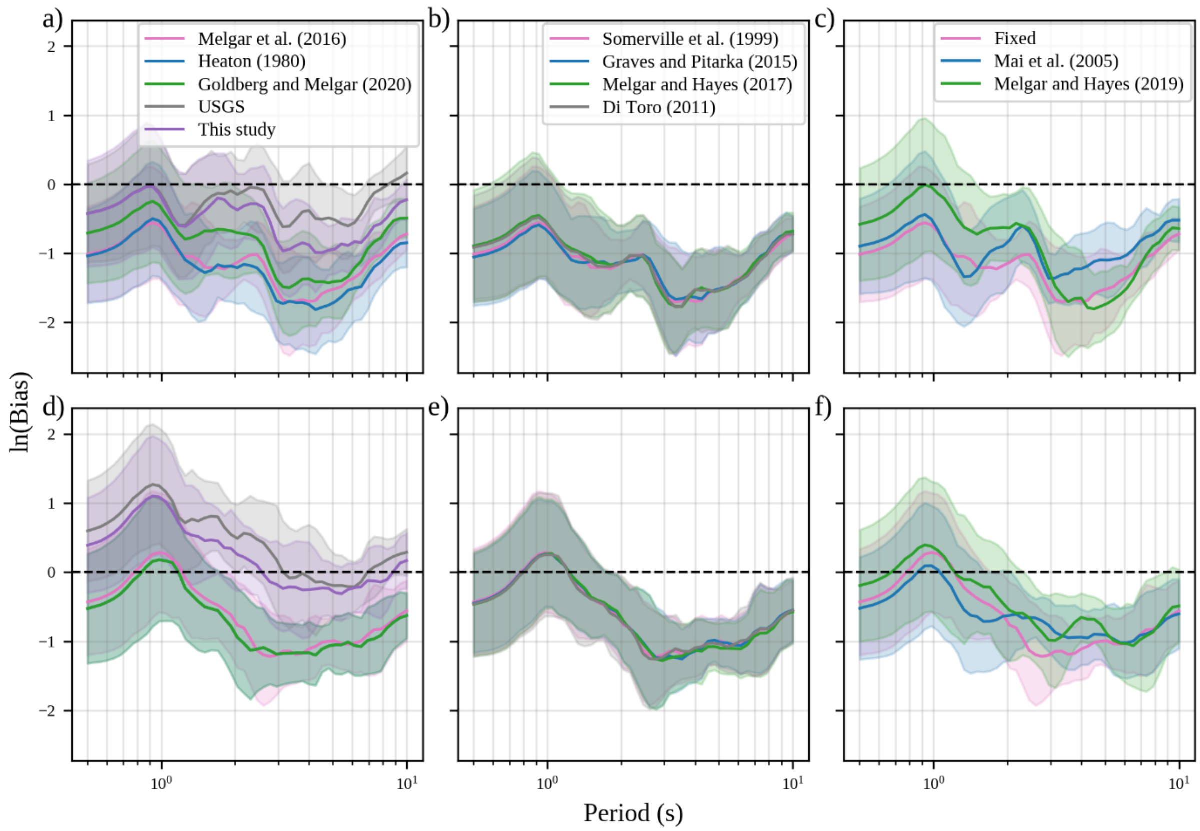

Figure 6. Bias between synthetics and observed geometric-mean horizontal response spectra. Curves show the mean log-bias, and shaded areas are ± 1 Standard Deviation (SD) of residuals. Seismograms are band-pass filtered in the 0.1-1.0 Hz range: a-c) results using the CRUST 2.0 velocity model (Bassin et al., 2000) for rupture velocity (V_r), rise time (t_0) and hypocentre location cases, respectively; d–f) corresponding results using the Central Chile velocity model (Caballero et al., 2023). a), d) only V_r is varied while t_0 is fixed to Somerville et al. (1999) and the hypocentre location is fixed to the observed Illapel earthquake; b), e) only t_0 is varied while V_r is fixed to Melgar et al. (2016) and the hypocentre remains fixed; c), f), only the hypocentre location is varied while V_r is fixed to Melgar et al. (2016) and t_0 to Somerville et al. (1999).

To quantify the sensitivity of each parameter, we compute three metrics (Table 1): mean ln(bias), Bias Factor, and RMSE. The mean ln(bias) describes whether the simulations systematically overestimate (negative values), underestimate (positive values) or unbiased (near zero values) the observed response spectra. The Bias Factor provides similar information, but values close to one represent minimal bias. The RMSE quantifies the overall accuracy of the synthetic spectra.

For the CRUST 2.0 velocity model, we observe the largest variability across the V_r formulations, consistent with the strong epistemic uncertainty shown in Figure 6. The USGS case provides the best central tendency, with a mean ln(bias) of –0.238 and a Bias Factor of 0.788, both slightly overestimating the observed response spectra. However, the RMSE of the simulations associated to this velocity model is the lowest with 0.29769, indicating good accuracy.

In contrast, the use of the Central Chile velocity model significantly reduces this variability. Across all V_r formulations, our preferred case performs best, with a mean ln(bias) of 0.088 and a Bias Factor of 1.092, both of which are very close to unity, while also producing the lowest RMSE of this velocity model with 0.35623, which is slightly higher than the USGS case in the CRUST2.0 model. Heaton (1980), the commonly used V_r assumption, yields essentially the same metrics as Goldberg and Melgar (2020). This indicates that, when the Central Chile velocity model is used, the variability associated with choosing between these two formulations is limited.

The t_0 cases behave similarly across all formulations, matching the low variability seen in Figure 6. This result further confirms that the t_0 formulations is not a major source of uncertainty in the ground-motion simulations, particularly when using a regional velocity model.

The hypocentre location cases show intermediate sensitivity, as shown in Figure 6. Under CRUST 2.0, the Melgar and Hayes (2019) case produces the lowest RMSE (0.41957), while the Mai et al. (2005) case shows the strongest bias (-0.85705). However, the three cases notably perform similar. Under the Central Chile model, all three formulations are comparable too, with narrow ln(bias) ranges (0.69 to 0.55), Bias Factors around 0.5, and only minor variations in

RMSE between the Fixed and Melgar and Hayes (2019) cases, principally. This indicates that hypocentre assumptions become less influential when using a regional velocity model. Although we evaluate the fixed case, it does not inform decisions for future events because it corresponds to the true hypocentre of the studied earthquake. Instead, it serves as a reference to determine which formulation best reproduces the observed ground-motion.

Table 1. Bias and error metrics comparison for different rupture velocity (V_r), rise time(t_0) and hypocentre cases.

Case	Kinematic parameter	Velocity model	Mean ln(bias)	Bias Factor	RMSE
Melgar et al. (2016)	V_r	CRUST 2.0	-1.11373	0.32833	0.52971
Heaton (1980)	V_r	CRUST 2.0	-1.20819	0.29874	0.54028
Goldberg and Melgar (2020)	V_r	CRUST 2.0	-0.85255	0.42633	0.37547
USGS: Goldberg et al. (2022)	V_r	CRUST 2.0	-0.23801	0.78819	0.29769
This study	V_r	CRUST 2.0	-0.56406	0.56890	0.31830
Melgar et al. (2016)	V_r	Central Chile	-0.69149	0.50083	0.39988
Heaton (1980)	V_r	Central Chile	-0.76444	0.46560	0.39725
Goldberg and Melgar (2020)	V_r	Central Chile	-0.76444	0.46560	0.39725
USGS: Goldberg et al. (2022)	V_r	Central Chile	0.28138	1.32496	0.36655
This study	V_r	Central Chile	0.08815	1.09215	0.35623
Sommerville et al. (1999)	t_0	CRUST 2.0	-1.11373	0.32833	0.52971
Graves and Pitarka (2015)	t_0	CRUST 2.0	-1.11526	0.32783	0.50624
Melgar and Hayes (2017)	t_0	CRUST 2.0	-1.06476	0.34481	0.48680
Di Toro (2011)	t_0	CRUST 2.0	-1.08481	0.33797	0.49410
Sommerville et al. (1999)	t_0	Central Chile	-0.69149	0.50083	0.39988
Graves and Pitarka (2015)	t_0	Central Chile	-0.70483	0.49419	0.39637
Melgar and Hayes (2017)	t_0	Central Chile	-0.72149	0.48603	0.39791
Di Toro (2011)	t_0	Central Chile	-0.70062	0.49628	0.40925
Fixed	Hypocentre	CRUST 2.0	-1.11373	0.32833	0.52971
Mai et al. (2005)	Hypocentre	CRUST 2.0	-0.85705	0.42441	0.50832
Melgar and Hayes (2019)	Hypocentre	CRUST 2.0	-0.92372	0.39704	0.41957
Fixed	Hypocentre	Central Chile	-0.69149	0.50083	0.39988

Mai et al. (2005)	Hypocentre	Central Chile	-0.67611	0.50859	0.52971
Melgar and Hayes (2019)	Hypocentre	Central Chile	-0.55218	0.57569	0.37298

3.2. Comparison between observed and synthetic data

After understanding the epistemic uncertainties involved in the simulation cases, we compare the geometric-mean response spectra of the synthetic and observed horizontal acceleration components. This comparison enables us to assess how each rupture formulation affects the ground-motion across the eight near-field stations. Figures 7 and 8 show such comparisons for each rupture parameter case and for both 1D velocity models.

Figures 7a and 8a show the greatest variability, confirming the high sensitivity and uncertainty associated with V_r. As seen in Figures 4a, 4d and Table 1, Melgar et al. (2016) and Heaton (1980) produce nearly identical rupture propagation. This similarity is also reflected in the response spectra, which closely align, especially when using the Central Chile velocity model (Figure 8a). In contrast, the other V_r formulations cover a broader amplitude range. The USGS model and the formulation introduced in this study match the observations more closely in both velocity models, suggesting that slower V_r values may provide a better representation of the rupture for this event.

Figures 7b and 8b show the t_0 variations where the synthetic spectra do not match the observations, consistent with the strong influence of the Melgar et al. (2016) model, which is fixed in these variations. However, the spectra from the different t_0 formulations remain tightly clustered. This behaviour is unexpected given the large differences in the t_0 distributions (Figures 4b and 4e) and indicates that t_0 exerts only a minor influence on the predicted ground-motion.

Figures 7c and 8c show some variability in the hypocentre location cases, although the differences are smaller than those in the V_r cases. Moreover, the response spectra obtained from the fixed hypocentre are quite similar to those of the Mai et al. (2005) and Melgar and Hayes (2019), despite being in clearly different positions and producing different directivity effects. These results are consistent with the uncertainty metrics in Table 1, which suggest that both heuristic approaches provide reasonable nucleation points for future scenario modelling.

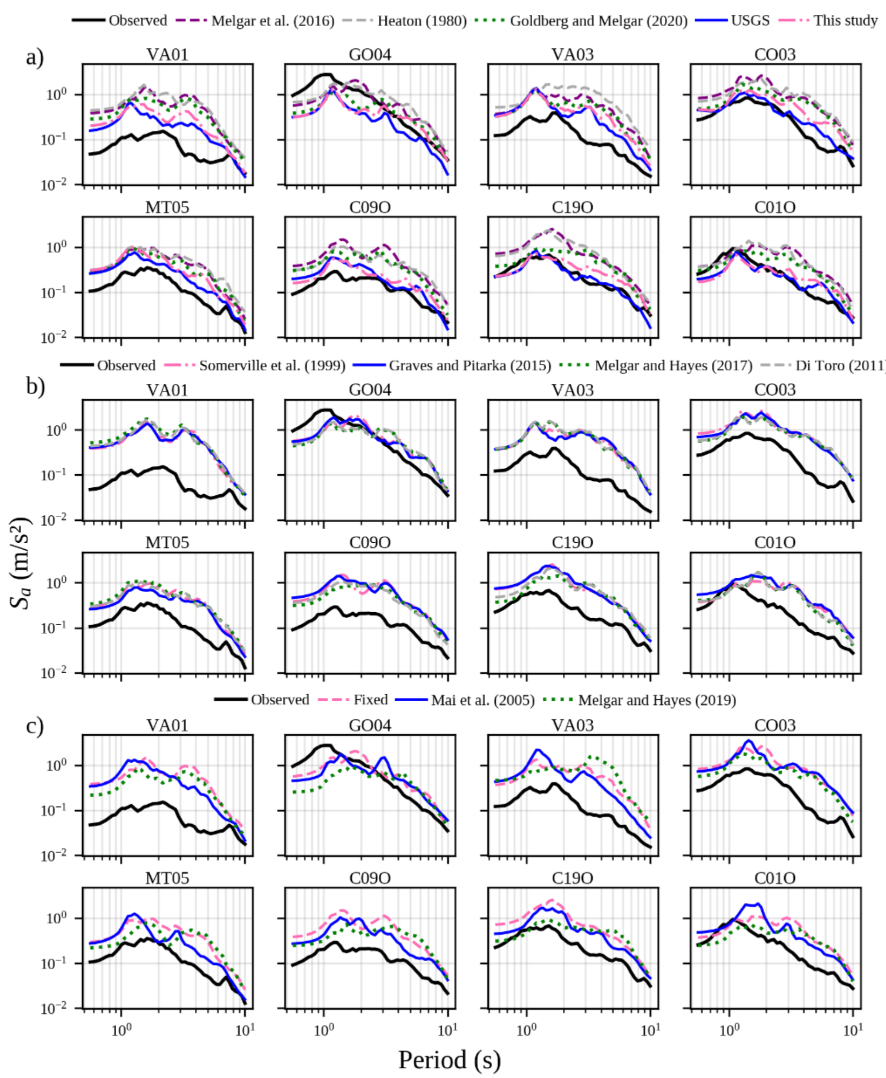

Figure 7. Comparison between observed and synthetic geometric-mean response spectral accelerations for every case: a) rupture velocity (V_r); b) rise time (t_0) and c) hypocentre location cases using the CRUST 2.0 1D velocity model (Bassin et al., 2000). Results are shown for a band-pass filtered frequency range of 0.1–1.0 Hz across the eight near-field stations.

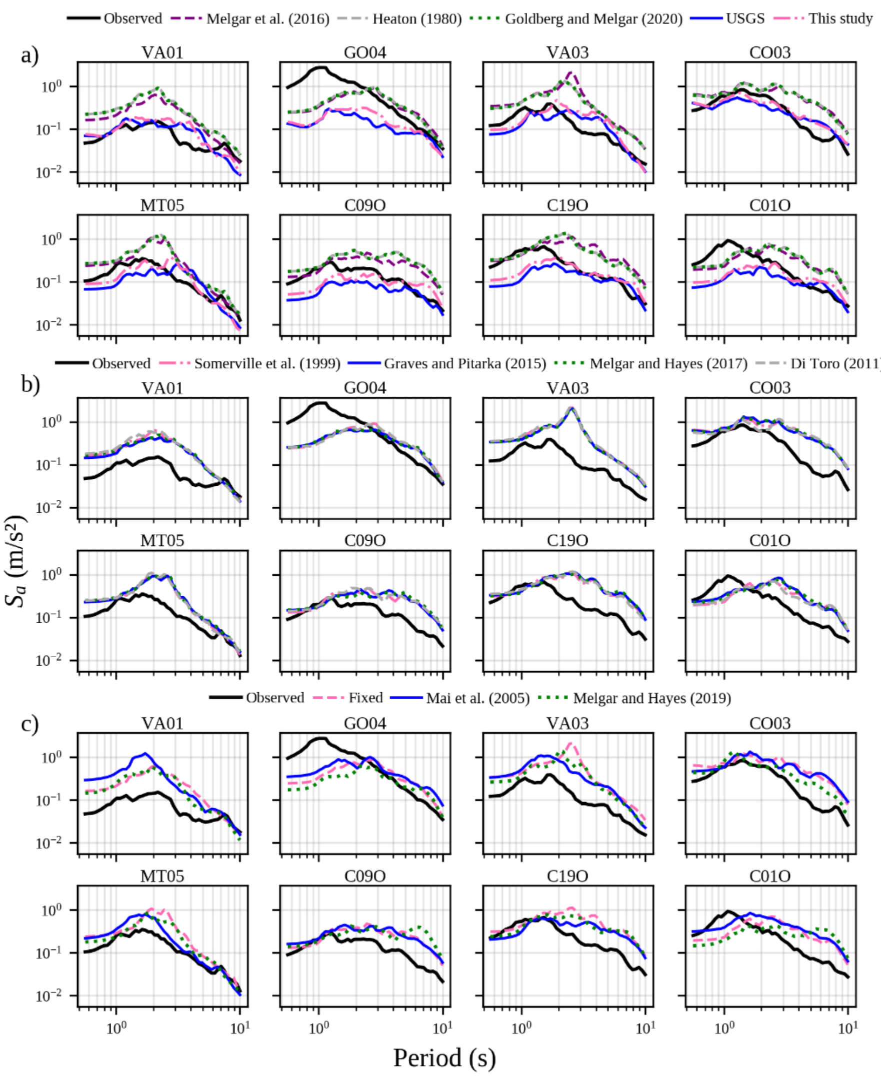

Figure 8. Comparison between observed and synthetic geometric-mean response spectral accelerations for every case: a) rupture velocity (V_r); b) rise time (t_0) and c) hypocentre location using the Central Chile 1D velocity model (Caballero et al., 2023). Results are shown for a band-pass filtered frequency range of 0.1–1.0 Hz across the eight near-field stations.

Additionally, we compare the observed acceleration waveforms with the best-fitting logic-tree branch synthetics. This branch has the lowest bias (mean ln $(bias)$ closest to zero) and a low RMSE. In particular, we use the 1-D velocity model of Central Chile, the V_r formulation proposed in this study, the Somerville et al. (1999) as the t_0 model, and the observed hypocentre location of the Illapel earthquake, corresponding to the fixed case.

Figure 9 shows the comparison of observed and synthetic acceleration waveforms in a bandpass filter frequency range of 0.1 to 1 Hz for the eight near-field stations used in this analysis. The comparison provides a direct measure of how closely the selected branch reproduces the observed waveform amplitudes and durations across the three components.

Overall, the simulations closely reproduce the main features of the recordings, including the waveform similarity, spectral content and amplitude. The best agreement is obtained at the rock stations VA01, VA03 and C19O. On the vertical components at VA01 and VA03, the synthetics tend to exceed the observations, with an overestimation associated with the main pulses. In contrast, GO04 and C01O show a clear underestimation, most notably at GO04 and mainly on the horizontal components. This mismatch may reflect local site effects that are not captured by the 1D velocity structure adopted here, and it could also indicate more complex (potentially nonlinear) site behaviour at GO04. However, MT05, which is also located in soil, shows the opposite tendency; the horizontal components are captured well by the simulations, while the vertical component exhibits a moderate overestimation of the main pulse.

Although we rely on a single event to quantify uncertainty, this comparison suggests that the selected best-fitting branch captures the characteristics of the near-field ground-motion time histories for a large megathrust earthquake, such as the Illapel event.

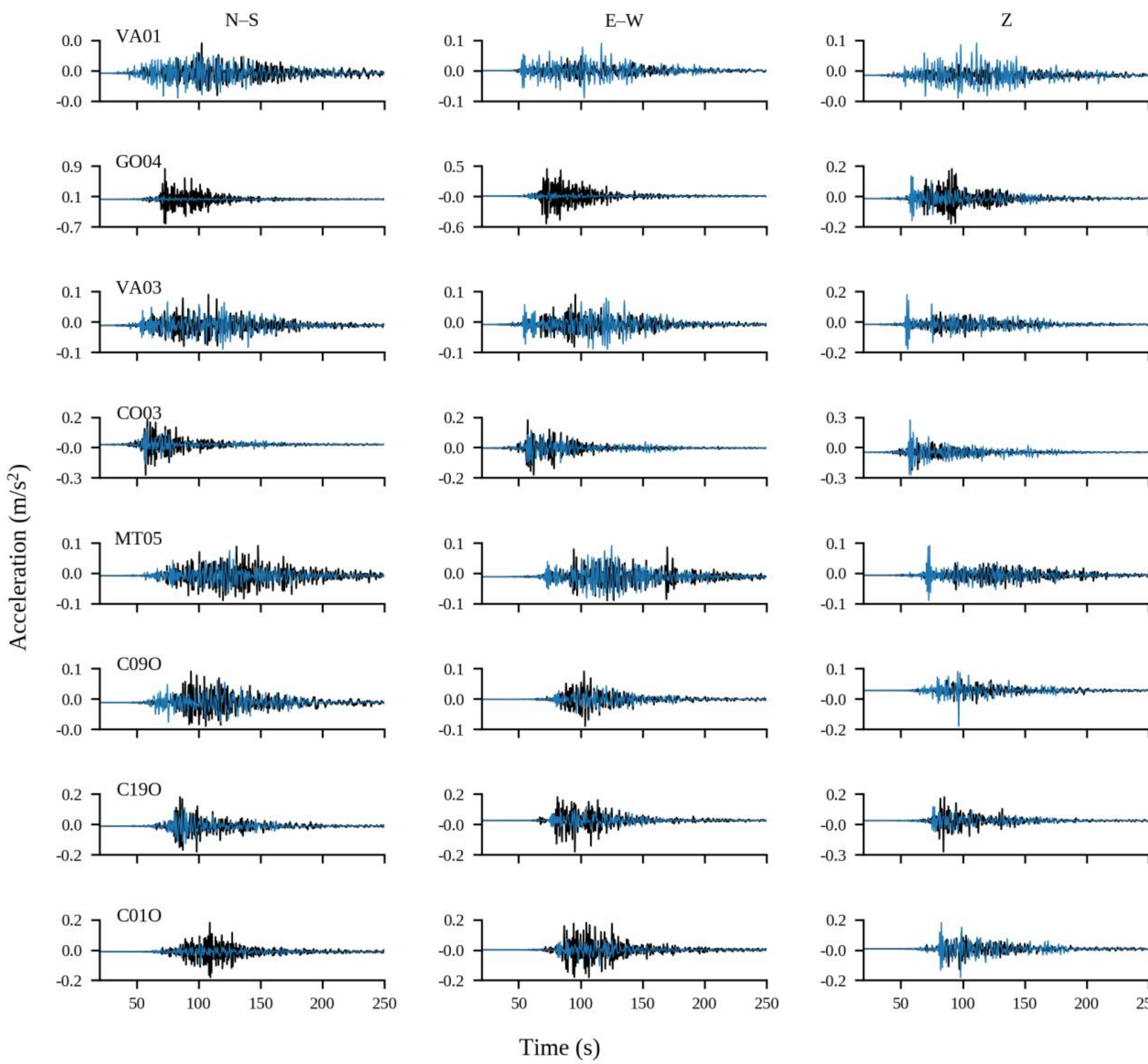

Figure 9. Comparison of observed (black) and synthetic acceleration (blue) waveforms for the Mw 8.3 Illapel earthquake at eight near-field stations. Waveforms are band-pass filtered between 0.1 to 1 Hz. Synthetics correspond to the best-fitting logic-tree branch using the Central Chile 1D velocity model, the V_r formulation proposed in this study, the t_0 according by Somerville et al. (1999), and the observed (fixed) hypocentre location.

In addition to these comparisons, we then test whether a single event, such as the 2015 Illapel earthquake, can capture the variability needed to constrain future scenarios. Figure 10 shows the mean synthetic and observed PGA and SA at 0.5, 2.0, and 10.0 s across all parameter variations.

PGA and SA at 0.5 and 2.0 s follow lognormal distributions (Figures 10a-c), while SA at 10 s exhibits much heavier tails and is better described by a Cauchy distribution (Figure 10d). The observed PGA (0.19 m/s²) and SA at 0.5 s (0.24 m/s²) fall near the central tendency of the synthetic realisations, indicating that one well-recorded event can capture short-period variability. However, the observed SA at 2.0 s (0.42 m/s²) lies somewhat off the distribution mean (Figure 10c), and the observed SA at 10 s (0.02 m/s²) falls in the extreme tail of the fitted Cauchy PDF (Figure 10d). These results suggest that a single event is insufficient to represent the spectral acceleration in long-period beyond about 2 s, which limits its use for future long-period scenario development.

Extending this analysis to multiple subduction earthquakes would broaden the range of rupture behaviours and help to reduce the epistemic uncertainties. Because this study focuses on uncertainties from the kinematic rupture process, future work should also assess the epistemic variability introduced by stochastic slip distribution generation schemes.

3.3. Evaluation of Frequency Reliability in Ground-Motion Modelling

We complete this study by evaluating the reliability of the computed frequency content, an aspect often overlooked in rupture model generators. We calculate the mean SD of residuals and the bias factor for the lowest-uncertainty formulation within each velocity model (Figure 11). For CRUST 2.0, we adopt the V_r from the USGS model, the t_0 from Melgar and Hayes (2017) formulation and a fixed hypocentre location. For the Central Chile model, we use the V_r inferred in this study, the t_0 from Somerville et al. (1999) and the same fixed hypocentre.

Because source resolution depends on the lowest V_s and the target frequency computed, the CRUST 2.0 model supports frequencies for the studied earthquake up to 5 Hz, with a corresponding spatial resolution of 48 m. In contrast, the Central Chile model reaches 10 Hz with a resolution of 60 m. Across the computed frequency range, the mean SD of residuals increases for both models. The bias factor approaches one, indicating minimal bias, near 2 Hz for CRUST 2.0 and remains stable around 3 Hz for Central Chile before decaying. The behaviour of the SD of residuals across the computed frequencies aligns with Pilz et al. (2025), confirming that 1D models remain reliable below 3 Hz, which represents the site-source conditions for this earthquake.

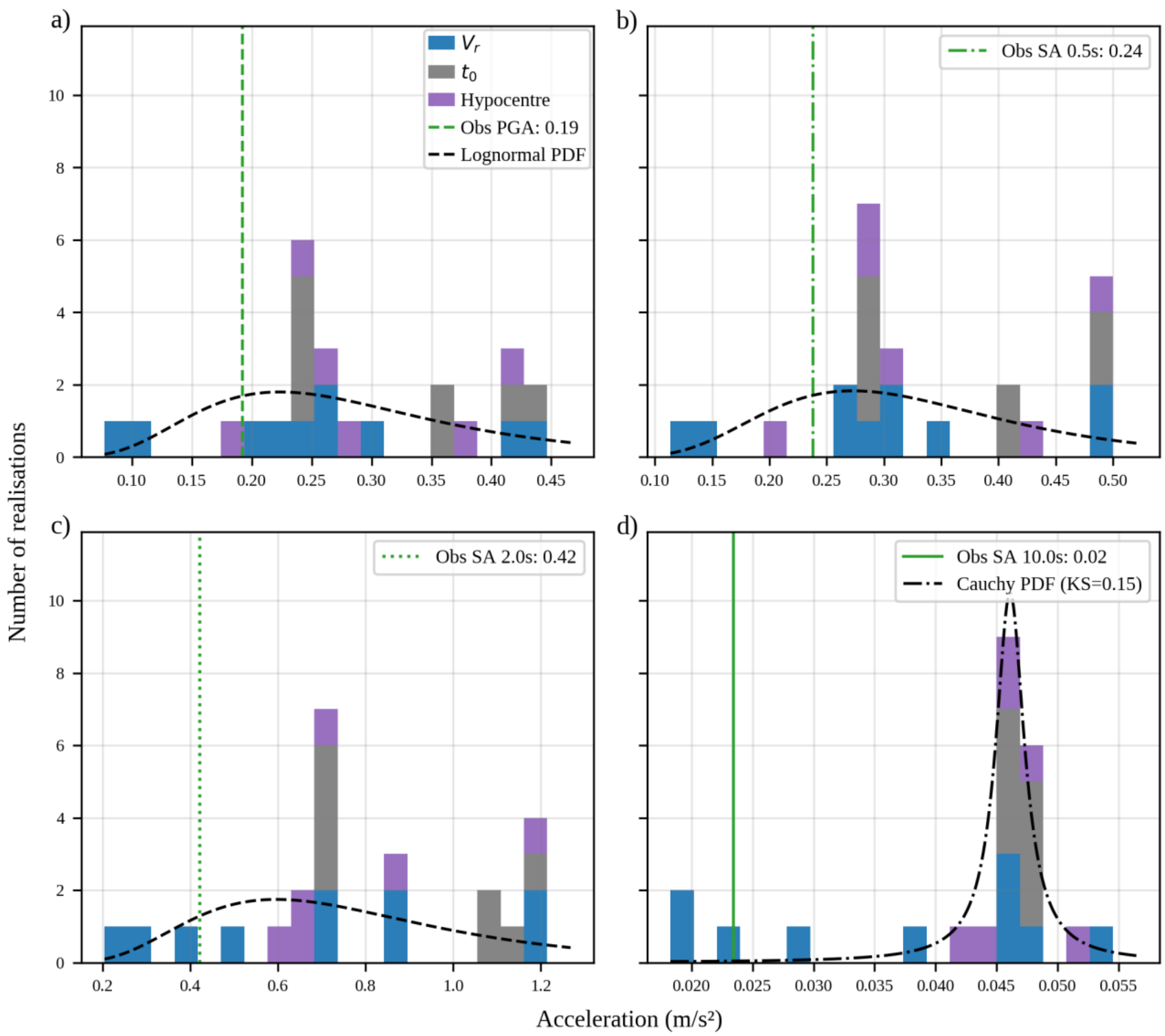

Figure 10. Histograms of mean horizontal geometric-mean synthetic, for the 24 realisations of the logic-tree framework, and observed acceleration values: a) distribution of simulated peak

ground acceleration (PGA); b) spectral accelerations (SA) at 0.5 s, c) 2.0 s, and d) 10.0 s. The bars show the results grouped according to the defined cases of variation in rupture velocity (V_r), rise time (t_0), and hypocentre location. Vertical green lines correspond to the observed mean values for each period. The black dashed and dash-dotted lines represent the best-fitting lognormal and Cauchy probability density functions (PDFs), respectively.

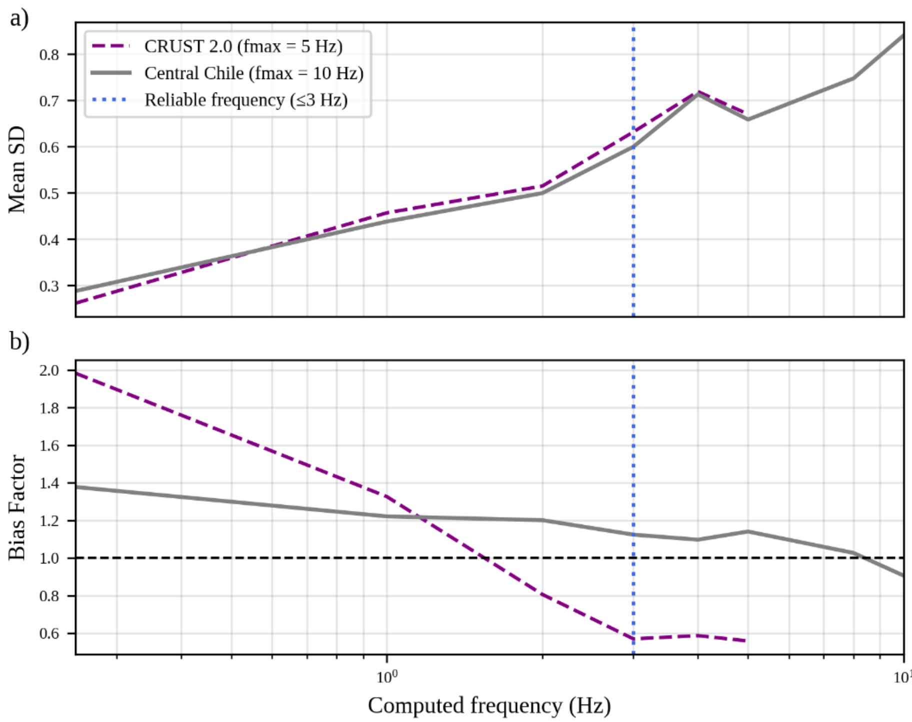

Figure 11. Uncertainty quantification of the computed frequency response for the two 1D velocity models analysed. For CRUST 2.0, we use a rupture velocity (V_r), from USGS (Goldberg et al., 2022), a rise time (t_0) from Melgar and Hayes (2017), and a fixed hypocentre location. For the Central Chile model, we use the (V_r), inferred in this study, a t_0 from Somerville et al. (1999), and a fixed hypocentre: a) mean Standard Deviation (SD) of residuals and b) Bias Factor. The green dotted line marks the reliable frequency range (≤ 3 Hz), which effectively captures the site response according to Pilz et al. (2025).

4. Conclusions

We quantify epistemic uncertainties in ground-motion simulations derived from kinematic rupture models based on slip distributions of large subduction earthquakes. Using the 2015 Illapel Mw 8.3 event as a case study, we test multiple formulations of rupture velocity (V_r), to constrain rupture time (t_{rup}), rise time (t_0), and hypocentre location across two one-dimensional (1D) velocity models. We evaluate their effects on simulated ground-motions at eight near-field stations by comparing synthetic and observed geometric-mean response spectra. We further assess how well the records of a single event are captured by the range of simulated intensity measures, and finally, we analyse the frequency reliability of the simulations across both 1D velocity models.

The main conclusions are:

- The V_r formulations produce the greatest variability in the ground-motion simulations. The behaviour of the mean ln(bias), Bias Factor, and mean RMSE confirms that V_r is the dominant source of epistemic uncertainty. The depth-dependent V_r formulation, proposed here, with $0.3V_s$ at depths <10 km and $0.5V_s$ at depths >15 km, minimises the uncertainty metrics for this particular case, especially when combined with the Central Chile velocity model.
- Despite the strong differences in the spatial distributions of t_0, the impact on ground-motion remains negligible. All metrics stay stable across formulations, indicating that t_0 does not substantially influence the predicted ground-motion.
- Hypocentre location has a moderate influence on the simulated ground-motion, and this effect becomes much smaller when we use the Central Chile velocity model. This

indicates that the influence of hypocentre assumptions depends on the choice of velocity model.

- Our frequency analysis shows that the simulations are reliable until 3 Hz. This confirms that 1D velocity models are adequate for representing low to intermediate frequencies in ground-motion modelling but not high frequencies, even if the computational resolution makes high-frequency computation feasible.
- The ground-motions of the well-recorded 2015 Illapel subduction earthquake in Central Chile are better captured by the range of the models at intermediate frequencies (0.5-0.3Hz) rather than at low frequencies (<0.5Hz).
- Overall, the results show that the regional velocity model (Central Chile) provides the best performance. Further refinement of regional velocity models is therefore a key pathway to reduce epistemic variability in ground-motion simulations
- Our final goal is not only to evaluate epistemic uncertainty but also to decrease it. The lowest-uncertainty models identified here provide a basis for simulating future synthetic earthquake scenarios to analyse aleatory variability in a way that complements the epistemic uncertainty evaluated in this study. However, because our analysis is based on a single earthquake, additional observations are necessary to more accurately calibrate and represent the rupture velocities for future simulations of large subduction earthquakes. This remains difficult in subduction zones with few well-recorded tsunamigenic earthquakes By reducing epistemic uncertainty in the kinematic rupture propagation, used to simulate ground-motion, our proposed framework supports a more physics-based seismic source integration for seismic-tsunami hazard assessment in subduction zones.

Data and Resources

The dataset and codes generated for this study are available at: https://github.com/monsebo/Kinematic-Rupture-From-a-Slip-Distribution-.git

The codes were implemented using Python 3 (Van Rossum and Drake, 2009), Pyrocko and its Fomosto module (Heimann et al., 2019). The slip distribution was used from the USGS inversion in https://earthquake.usgs.gov/earthquakes/eventpage/us20003k7a/finite-fault (last accessed on 30 November 2025).

Acknowledgments

A.M. Buenrostro acknowledges funding from the National Agency of Research and Development (ANID) under the National Doctoral Scholarship 21210775, the Pyrocko development team, especially Sebastian Heimann, for his assistance in reviewing the implementation of the Fomosto module and the combi-source used to compute the ground-motion simulations, as well as Emanuel Caballero for kindly providing the velocity model used in this study. J. Jara acknowledges partial funding from the Marie Skłodowska-Curie Postdoctoral Fellowship (grant no. 101066069) and the Volkswagen Foundation (grant no. 0200087-00). A.M. Buenrostro, J.G.F. Crempien and R. Jünemann also acknowledge funding from grants ANID/Anillo ACT240044 and Center for Interdisciplinary Research on Disaster Risk, Resilience and Recovery (CIGIDEN R+), ANID/CIN250023.

References

Andrews, D. J., 2005, Rupture dynamics with energy loss outside the slip zone, J Geophys Res Solid Earth, 110, no. 1, 1–14, doi: 10.1029/2004JB003191.

Andrews, D. J., 1976, RUPTURE VELOCITY OF PLANE STRAIN SHEAR CRACKS., J Geophys Res, 81, no. 32, 5679–5687, doi: 10.1029/JB081i032p05679.

Bassin, C., 2000, The current limits of resolution for surface wave tomography in North America, Eos Trans. AGU, 81, F897.

Buenrostro, A. M., F. Cotton, J. Jara, J. G. F. Crempien, and R. Jünemann, 2025, Synthetic Seismograms from Physics-based Modeling of Heterogeneous Rupture for Large Subduction Earthquakes, in EGU General Assembly 2025, Vienna, Austria, 27 Apr–2 May 2025, EGU25-6860.

Buenrostro, A. M., J. G. F. Crempien, R. Jünemann, A. Urrutia, F. Sahli Costabal, and J. Delpiano, 2026, Convolutional neural networks for tsunami intensity measure prediction from slip and coseismic deformation data, Eng Appl Artif Intell, 165, 113405, doi: 10.1016/j.engappai.2025.113405.

Caballero, E. et al., 2023, Revisiting the 2015 Mw = 8.3 Illapel earthquake: unveiling complex fault slip properties using Bayesian inversion, Geophys J Int, 235, no. 3, 2828–2845, doi: 10.1093/gji/ggad380.

Castro-Cruz, D., and P. M. Mai, 2025, A New Kinematic Rupture Generation Technique and Its Application, Geophys J Int, doi: 10.1093/gji/ggaf385.

Cienfuegos, R., P. A. Catalán, A. Urrutia, R. Benavente, R. Aránguiz, and G. González, 2018, What Can We Do to Forecast Tsunami Hazards in the Near Field Given Large Epistemic Uncertainty in Rapid Seismic Source Inversions?, Geophys Res Lett, 45, no. 10, 4944–4955, doi: 10.1029/2018GL076998.

Cotton, F., and M. Campillo, 1995, Frequency domain inversion of strong motions: application to the 1992 Landers earthquake, J Geophys Res, 100, no. B3, 3961–3975, doi: 10.1029/94JB02121.

Crempien, J. G. F., and R. J. Archuleta, 2017, Within-Event and Between-Events Ground Motion Variability from Earthquake Rupture Scenarios, Pure Appl Geophys, 174, no. 9, 3451–3465, doi: 10.1007/s00024-017-1615-x.

Crempien, J. G. F., A. Urrutia, R. Benavente, and R. Cienfuegos, 2020, Effects of earthquake spatial slip correlation on variability of tsunami potential energy and intensities, Sci Rep, 10, no. 1, 8399, doi: 10.1038/s41598-020-65412-3.

De Risi, R., and K. Goda, 2016, Probabilistic earthquake–Tsunami multi-hazard analysis: Application to the tohoku region, Japan, Front Built Environ, 2, doi: 10.3389/fbuil.2016.00025.

Di Toro, G., R. Han, T. Hirose, N. De Paola, S. Nielsen, K. Mizoguchi, F. Ferri, M. Cocco, and T. Shimamoto, 2011, Fault lubrication during earthquakes, Nature, 471, no. 7339, 494–499, doi: 10.1038/nature09838.

Gabriel, A. A., J. P. Ampuero, L. A. Dalguer, and P. M. Mai, 2013, Source properties of dynamic rupture pulses with off-fault plasticity, J Geophys Res Solid Earth, 118, no. 8, 4117–4126, doi: 10.1002/jgrb.50213.

Gabriel, A. A., J. P. Ampuero, L. A. Dalguer, and P. M. Mai, 2012, The transition of dynamic rupture styles in elastic media under velocity-weakening friction, J Geophys Res Solid Earth, 117, no. 9, doi: 10.1029/2012JB009468.

Goda, K., R. De Risi, F. De Luca, A. Muhammad, T. Yasuda, and N. Mori, 2021, Multi-hazard earthquake-tsunami loss estimation of Kuroshio Town, Kochi Prefecture, Japan considering the Nankai-Tonankai megathrust rupture scenarios, International Journal of Disaster Risk Reduction, 54, doi: 10.1016/j.ijdrr.2021.102050.

Goda, K., T. Yasuda, N. Mori, and P. M. Mai, 2015, Variability of tsunami inundation footprints considering stochastic scenarios based on a single rupture model: Application to the 2011

Tohoku earthquake, J Geophys Res Oceans, 120, no. 6, 4552–4575, doi: 10.1002/2014JC010626.

Goldberg, D. E., P. Koch, D. Melgar, S. Riquelme, and W. L. Yeck, 2022, Beyond the Teleseism: Introducing Regional Seismic and Geodetic Data into Routine USGS Finite-Fault Modeling, Seismological Research Letters, 93, no. 6, 3308–3323, doi: 10.1785/0220220047.

Goldberg, D. E., and D. Melgar, 2020, Generation and validation of broadband synthetic p waves in semistochastic models of large earthquakes, Bulletin of the Seismological Society of America, 110, no. 4, 1982–1995, doi: 10.1785/0120200049.

Graves, R. W., and A. Pitarka, 2010, Broadband ground-motion simulation using a hybrid approach, Bulletin of the Seismological Society of America, 100, no. 5 A, 2095–2123, doi: 10.1785/0120100057.

Graves, R., and A. Pitarka, 2016, Kinematic ground-motion simulations on rough faults including effects of 3D stochastic velocity perturbations, Bulletin of the Seismological Society of America, 106, no. 5, 2136–2153, doi: 10.1785/0120160088.

Graves, R., and A. Pitarka, 2015, Refinements to the Graves and Pitarka (2010) broadband ground-motion simulation method, Seismological Research Letters, 86, no. 1, 75–80, doi: 10.1785/0220140101.

Guatteri, M., and M. Cocco, 1996, On the Variation of Slip Direction during Earthquake Rupture: Supporting and Conflicting Evidence from the 1989 Loma Prieta Earthquake.

Guatteri, M., P. M. Mai, and G. C. Beroza, 2004, A Pseudo-Dynamic Approximation to Dynamic Rupture Models for Strong Ground Motion Prediction.

Hartzell, S., 1989, Comparison of seismic waveform inversion results for the rupture history of a finite fault: application to the 1986 North Palm Springs, California, earthquake, J Geophys Res, 94, no. B6, 7515–7534, doi: 10.1029/JB094iB06p07515.

Heaton, T. H., 1990, Evidence for and implications of self-healing pulses of slip in earthquake rupture.

Heimann, S., H. Vasyura-Bathke, H. Sudhaus, M. Paul Isken, M. Kriegerowski, A. Steinberg, and T. Dahm, 2019, A Python framework for efficient use of pre-computed Green's functions in seismological and other physical forward and inverse source problems, Solid Earth, 10, no. 6, 1921–1935, doi: 10.5194/se-10-1921-2019.

Herrero, A., and P. Bernard, 1994, A Kinematic Self-Similar Rupture Process for Earthquakes.

Kagawa, T., K. Irikura, and P. G. Somerville, 2004, Differences in ground motion and fault rupture process between the surface and buried rupture earthquakes.

Kurahashi, S., and K. Irikura, 2013, Short-period source model of the 2011 Mw 9.0 Off the Pacific Coast of Tohoku earthquake, Bulletin of the Seismological Society of America, 103, no. 2 B, 1373–1393, doi: 10.1785/0120120157.

Løvholt, F., S. Glimsdal, C. B. Harbitz, N. Zamora, F. Nadim, P. Peduzzi, H. Dao, and H. Smebye, 2012, Tsunami hazard and exposure on the global scale, Earth Sci Rev, 110, nos. 1–4, 58–73, doi: 10.1016/j.earscirev.2011.10.002.

Løvholt, F., G. Pedersen, C. B. Harbitz, S. Glimsdal, and J. Kim, 2015, On the characteristics of landslide tsunamis, Royal Society of London.

Madariaga, R., K. Olsen, and R. Archuleta, 1998, Modeling Dynamic Rupture in a 3D Earthquake Fault Model.

Mai, P. M., P. Spudich, and J. Boatwright, 2005, Hypocenter locations in finite-source rupture models, Bulletin of the Seismological Society of America, 95, no. 3, 965–980, doi: 10.1785/0120040111.

Meier, M.-A., J. P. Ampuero, and T. H. Heaton, 2017, The hidden simplicity of subduction megathrust earthquakes.

Melgar, D., and G. P. Hayes, 2017, Systematic Observations of the Slip Pulse Properties of Large Earthquake Ruptures, Geophys Res Lett, 44, no. 19, 9691–9698, doi: 10.1002/2017GL074916.

Melgar, D., and G. P. Hayes, 2019, The correlation lengths and hypocentral positions of great earthquakes, Bulletin of the Seismological Society of America, 109, no. 6, 2582–2593, doi: 10.1785/0120190164.

Melgar, D., R. J. LeVeque, D. S. Dreger, and R. M. Allen, 2016, Kinematic rupture scenarios and synthetic displacement data: An example application to the Cascadia subduction zone, J Geophys Res Solid Earth, 121, no. 9, 6658–6674, doi: 10.1002/2016JB013314.

Okada, Y., 1985, Surface deformation due to shear and tensile faults in a half-space, Bulletin of the Seismological Society of America, 75, no. 4, 1135–1154, doi: 10.1785/BSSA0750041135.

Park, H., D. T. Cox, M. S. Alam, and A. R. Barbosa, 2017, Probabilistic seismic and tsunami hazard analysis conditioned on a megathrust rupture of the cascadia subduction zone, Front Built Environ, 3, doi: 10.3389/fbuil.2017.00032.

Pilz, M., F. Cotton, and C. Zhu, 2025, Site-response high-frequency frontiers and the added value of site-specific earthquake record-based measurements of velocity and attenuation, Earthquake Spectra, 41, no. 2, 1151–1176, doi: 10.1177/87552930241311312.

Pitarka, A., R. Graves, K. Irikura, K. Miyakoshi, C. Wu, H. Kawase, A. Rodgers, and D. McCallen, 2022, Refinements to the Graves–Pitarka Kinematic Rupture Generator, Including a Dynamically Consistent Slip-Rate Function, Applied to the 2019 Mw 7.1 Ridgecrest Earthquake, Bulletin of the Seismological Society of America, 112, no. 1, 287–306, doi: 10.1785/0120210138.

Riquelme, S., H. Schwarze, M. Fuentes, and J. Campos, 2020, Near-Field Effects of Earthquake Rupture Velocity Into Tsunami Runup Heights, J Geophys Res Solid Earth, 125, no. 6, doi: 10.1029/2019JB018946.

Ruiz, J. A., D. Baumont, P. Bernard, and C. Berge-Thierry, 2011, Modelling directivity of strong ground motion with a fractal, k-2, kinematic source model, Geophys J Int, 186, no. 1, 226–244, doi: 10.1111/j.1365-246X.2011.05000.x.

Scala, A. et al., 2020, Effect of Shallow Slip Amplification Uncertainty on Probabilistic Tsunami Hazard Analysis in Subduction Zones: Use of Long-Term Balanced Stochastic Slip Models, Pure Appl Geophys, 177, no. 3, 1497–1520, doi: 10.1007/s00024-019-02260-x.

Small, D. T., and D. Melgar, 2023, Can Stochastic Slip Rupture Modeling Produce Realistic M9+ Events?, J Geophys Res Solid Earth, 128, no. 3, doi: 10.1029/2022JB025716.

Somerville, P., K. Irikura, R. Graves, S. Sawada, D. Wald, N. Abrahamson, G. Institute, and J. N. Smith, n.d., Characterizing Crustal Earthquake Slip Models for the Prediction of Strong Ground Motion Yoshinori Iwasaki Takao Kagawa.

Spudich, P., and R. J. ARCHULETA, 1987, Techniques for Earthquake Ground-Motion Calculation with Applications to Source, Seismic strong motion synthetics, 4, 205.

Van Rossum, G., and F. L. Drake, 2009, Introduction to PYTHON 2.6, CreateSpace, Scotts Valley, CA.

Venegas-Aravena, P., 2023, Geological earthquake simulations generated by kinematic heterogeneous energy-based method: Self-arrested ruptures and asperity criterion, Open Geosciences, 15, no. 1, doi: 10.1515/geo-2022-0522.

Yokota, Y., K. Koketsu, Y. Fujii, K. Satake, S. Sakai, M. Shinohara, and T. Kanazawa, 2011, Joint inversion of strong motion, teleseismic, geodetic, and tsunami datasets for the rupture process of the 2011 Tohoku earthquake, Geophys Res Lett, 38, no. 24, doi: 10.1029/2011GL050098.